2012

Height dependent laser metal deposition process modeling

Patrick M. Sammons

Department:

HEIGHT DEPENDENT LASER METAL DEPOSITION PROCESS MODELING

by

PATRICK MICHAEL SAMMONS

A THESIS

Presented to the Faculty of the Graduate School of the

MISSOURI UNIVERSITY OF SCIENCE AND TECHNOLOGY

In Partial Fulfillment of the Requirements for the Degree

MASTER OF SCIENCE IN MECHANICAL ENGINEERING

2012

Approved by

Douglas A. Bristow, Advisor
Robert G. Landers, Advisor
Frank W. Liou

PUBLICATION THESIS OPTION

This thesis has been prepared in the style utilized by the ASME Journal Of Manufacturing Science and Engineering. Pages 4-38 are intended for submission publication that journal.

ABSTRACT

Laser Metal Deposition (LMD) is used to construct functional parts in a layer-by-layer fashion. The heat transfer from the melt region to the solid region plays a critical role in the resulting material properties and part geometry. The heat transfer dynamics can change significantly as the layers increase, depending on the geometry of the sub layers. However, this effect is unaccounted for in previous analytical models, which are only valid for a single layer. This thesis develops a layer dependent model of the LMD process for the purpose of designing advanced layer-to-layer controllers. A lumped-parameter model of the melt pool is introduced and then extended to include elements that capture height dependent effects on the melt pool dimensions and temperature. The model dynamically relates the process inputs (e.g., laser power, material mass flow rate, and scan speed) to the melt pool dimensions and temperature. A finite element analysis is then conducted to determine the effect of scan speed and track height on the solid region temperature gradient at the melt pool solidification boundary. Experimental results demonstrate that the model successfully predicts multilayer phenomenon for two deposits on two different substrates. Finally, an investigation into the sensitivity of track width to changes in process parameters is conducted.

ACKNOWLEDGEMENTS

I would like to thank Dr. Doug Bristow and Dr. Robert G. Landers for their guidance in completion of this work. I would also like to thank Dr. Frank Liou for the use of the LAMP laboratory and the resources therein and Todd Sparks for help with the experimental work presented in this thesis.

TABLE OF CONTENTS

Page

LIST OF ILLUSTRATIONS

Page

LIST OF TABLES

Page

1. INTRODUCTION

Laser Metal Deposition (LMD) is an additive manufacturing process that allows parts to be built using three dimensional CAD models [1]. Unlike traditional machining where material is removed to produce the desired structure, LMD builds the part layer by layer. In LMD, a laser is used to create a molten pool to which solid material in the form of feed stock or metal powder is added. As material is added to the molten pool, a small bead consisting of melted material is formed. As the laser and solid material feed move away, the melt pool follows the laser allowing the previously formed melt pool to solidify. By moving the laser and material feed along a path, single layers are fabricated. The laser and material feed are then displaced in the vertical direction and the next layer of the part is deposited. Continuing in this fashion, parts of complex geometry are built.

It is important, as with any manufacturing process, to produce high-quality parts. For the LMD process, quality includes dimensional accuracy as well as suitable solidified material microstructure properties. The dimensional accuracy and microstructure properties are defined by melt pool morphology and melt pool temperature, respectively. Thus, to obtain parts with operator specified dimensions or desired microstructure properties, a closed-loop process controller should be used. Using a model of the LMD process that incorporates height dependency allows for the control multi-layer depositions producing structures with near-net shape properties.

2. LITERATURE REVIEW

The LMD process is dynamically complex and usually requires sophisticated models to describe the relationships between the process inputs (e.g., laser power, material mass flow rate, and scan speed) and the quantities of interest, which include the melt pool dimensions and temperature. Analytical models have been developed [2,3] using mass, momentum and energy balances across the melt pool, with and without the effects of phase change. These models are able to predict the melt pool morphology with dimensional accuracy for single layer tracks. The model developed in [4] uses alternate track profiles seen in experimental work to describe the single layer effects of process inputs on melt pool size and shape. In addition, more complex models based on finite element techniques describing the melt pool have been derived [4-7]. However, the complexities of these models require significant computational resources and are thus not suited for process control.

On the other hand, empirical models tend to lend themselves to process controller design because of their relatively simplicity, as in [8-11]. Additionally, they have been used accurately in multiple layer depositions [12]. However, because of their nature, empirical models require much experimental and system identification work to develop an accurate model.

3. OBJECTIVE

The objective of the work presented herein is to develop a model that is applicable to describing multi-layer depositions while maintaining the simplicity and intuitiveness of

current single layer models. By restricting the scope of the modeling, the developed model retains the ability to be used for process planning and closed-loop control design. This is an important aspect for a model such that it can be used to build structures with properties closer to those desired while minimizing any necessary post-processing.

I. HEIGHT DEPENDENT LASER METAL DEPOSITION PROCESS MODELING

ABSTRACT

Laser Metal Deposition (LMD) is used to construct functional parts in a layer-by-layer fashion. The heat transfer from the melt region to the solid region plays a critical role in the resulting material properties and part geometry. The heat transfer dynamics can change significantly as the layers increase, depending on the geometry of the sub layers. However, this effect is not taken into account in previous analytical models, which are only valid for a single layer. This thesis develops a layer dependent model of the LMD process for the purpose of designing advanced layer-to-layer controllers. A lumped-parameter model of the melt pool is introduced and then extended to include elements that capture height dependent effects on the melt pool dimensions and temperature. The model dynamically relates the process inputs (e.g., laser power, material mass flow rate, and scan speed) to the melt pool dimensions and temperature. A finite element analysis is then conducted to determine the effect of scan speed and track height on the solid region temperature gradient at the melt pool solidification boundary. An investigation into the sensitivity of track width to changes in the process parameters is conducted. Finally, experimental results demonstrate that the model successfully predicts multilayer phenomenon for two deposits on two different substrates.

1. INTRODUCTION

Laser Metal Deposition (LMD) is an additive manufacturing process that allows metal parts to be built using three dimensional CAD models [1]. Unlike traditional machining where material is removed to produce the desired structure, LMD builds the part layer by layer. In LMD, a laser is used to create a molten pool to which solid material in the form of feed stock or metal powder is added. As material is added to the molten pool, a small bead of melted material is formed. As the laser and solid material feed are displaced away, relative to the molten bead, the melt pool is allowed to solidify. By moving the laser and material feed along a path, single layers are fabricated. Then, subsequent layers are deposited to build parts of complex geometry.

The LMD process is complex and usually requires sophisticated models to describe the relationships between the process inputs (e.g., laser power, material mass flow rate, and scan speed) and the quantities of interest, which include the melt pool dimensions and temperature. Analytical models have been developed [2,3] using mass, momentum and energy balances across the melt pool, with and without the effects of phase change. These models are able to predict the melt pool morphology with dimensional accuracy for single layer tracks. The model developed in [4] uses alternate track profiles seen in experimental work to describe the single layer effects of process inputs on melt pool size and shape. In addition, more complex models based on finite element techniques describing the melt pool have been derived [4-7]. However, the complexity of these models requires significant computational resources and is thus not suitable for process control. On the other hand, empirical models, e.g., [8-11], tend to lend themselves to process planning and controller design because of their relatively

simplicity. Additionally, they have been used accurately in multiple layer depositions [12]. However, because of their nature, empirical models require much experimental and system identification work to develop an accurate model and are only applicable to the identified operation.

The LMD process is very sensitive to changes in the melt pool heat transfer. As the number of layers increases, conductive losses to sub layers can vary significantly. Thus, the use of a single layer model to predict or control multilayer builds can result in significant deviations from the expected result. The objective of this paper is to develop a multilayer model suitable for the development of LMD process plans and control systems.

This paper will first present a dynamic model that describes in-layer dynamics of a single layer track [2] based on lumped-parameter thermal, momentum and material balances at the melt pool boundary. This model is then augmented with a solidification term that incorporates height dependency. The developed model is then used to illustrate how melt pool morphology depends on model parameters, deposition setup, and process parameters, and that height dependent effects can be predicted. A comparison of the simulation results with experimental data validates the developed model.

2. LMD PHYSICS AND BACKGROUND

2.1. PROCESS DESCRIPTION AND SHAPE EQUATIONS

Laser Metal Deposition is a complex process governed by mass, thermal and fluid flow. While many complex interactions take place to form the resulting melt pool morphology, experimental results [13,14] indicate that the melt pool takes on the shape of

an oblate half ellipsoid The horizontal melt pool principal axes are the shape parameters length and width, and the vertical half axis, is the shape parameter height. Therefore, the melt pool volume and cross sectional area in the direction of deposition, respectively, are

$$V(t) = \frac{\pi}{6} w(t) h(t) l(t) \tag{1}$$

$$A_c(t) = \frac{\pi}{4} w(t) h(t) \tag{2}$$

where V is the melt pool volume (m^3), w is the melt pool width (m), h is the melt pool height (m), l is the melt pool length (m), and A_c is the melt pool cross sectional area in the direction of deposition (m^2). By convention, the front of the melt pool is assumed to lie at the same position as the laser, thus the melt pool length is

$$l(t) = d(t) - s(t) \tag{3}$$

where d is the laser position (m) and s is the solidification front (m). In reality, the melt pool will tend to lead the laser and therefore Eq. (3) represents an approximation of the melt pool length. The distance the melt pool leads the laser depends on the process parameters; however, it is assumed small when compared to the length.

The part is built on a substrate, as shown in Figure 1, that is located in a fixture and moves with a scan speed while the coaxial laser beam and powder flow rate systems are stationary above the melt pool. The solidified material is referred to as the solid

region and contains two portions. For a thin-walled part, the out-of-layer solidified material has length L_t and the in-layer solidified material has length s.

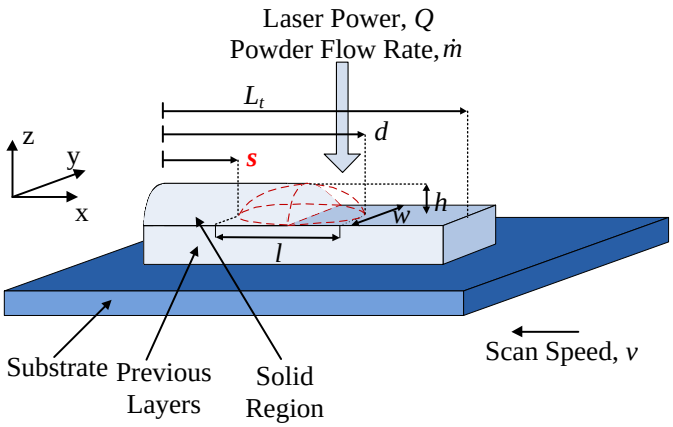

FIG. 1. SCHEMATIC SHOWING MELT POOL SHAPE PARAMETERS, SUBSTRATE, DIRECTION OF TRAVEL AND COORDINATE FRAME.

The model as derived in [2] describes a static relationship between melt pool width and length, based on laser power and melt pool temperature. This relationship is based on a solution to the steady-state three dimensional heat conduction equation with a moving point source. In addition, heat conducted to the substrate is lumped into a single, static term. While relating melt pool width and length in this fashion and lumping the heat losses to the substrate into a single term provides a relatively dimensionally accurate prediction of depositions for a single layer, it does not take into account any changes in the heat transfer characteristics that occur as the melt pool moves further from the substrate in the vertical direction. The development of the melt pool dynamic model in this paper follows closely to that given in [2] with one key difference. Here, the position

of the melt pool solidification front in the x-direction is treated as a free variable. An additional equation will be introduced later to model the solidification rate.

2.2. MASS, ENERGY, AND MOMENTUM BALANCES

The model in [2] is a dynamic, lumped-parameter description relating the process inputs, laser power, scan speed and material mass flow rate to melt pool length, width, height and temperature. The melt pool mass balance equation is

$$\frac{\partial}{\partial t}\underbrace{\left(\rho V(t)\right)}_{\text{Melt pool mass}} = \underbrace{\mu \dot{m}(t)}_{\substack{\text{Material added} \\ \text{by deposition}}} - \underbrace{\rho A_c(t)\dot{s}(t)}_{\substack{\text{Material lost to} \\ \text{solidification}}} \tag{4}$$

where ρ is the deposition material density (kg/m^3), $\dot{s}$ is the solidification rate in the direction of deposition at the back edge of the melt pool (m/s), μ is the powder catchment efficiency coefficient, and $\dot{m}$ is the powder mass flow rate (kg/s).

The change in melt pool momentum in the direction of deposition is a combination of the momentum of added material, momentum lost from solidifying material, and surface tension at the front of the melt pool in the direction of deposition. The material added to the melt pool has zero velocity in the direction of deposition (and thus zero momentum), while the material that is solidifying has a velocity equal to the scan speed. Thus, the melt pool momentum balance is

$$\frac{\partial}{\partial t}\underbrace{\left(\rho V(t)v(t)\right)}_{\text{Melt pool momentum}} = \underbrace{\rho A_c(t)\dot{s}(t)v(t)}_{\substack{\text{Momentum lost to} \\ \text{solidification}}} + \underbrace{[1-\cos(\theta)][\gamma_{GL}-\gamma_{SL}]w(t)}_{\text{Momentum lost to surface tension forces}} \tag{5}$$

where θ is the material wetting angle (rad), γ_{GL} and γ_{SL} are the material specific gas to liquid surface tension coefficient (N/m) and solid to liquid surface tension coefficient (N/m), respectively, and v is the scan speed (m/s). It should be noted that the parameters θ, γ_{GL} and γ_{SL} are highly material and temperature dependent. Finally, the melt pool energy balance is

$$\frac{\partial}{\partial t}\underbrace{\left(\rho V(t)e(t)\right)}_{\text{Melt pool energy}} = \underbrace{\mu\dot{m}(t)e_f}_{\substack{\text{Energy of}\\ \text{incoming powder}}} - \underbrace{\rho A_c(t)\dot{s}(t)e_b}_{\substack{\text{Energy of solidified}\\ \text{material}}} + \underbrace{\sum P_s(t)}_{\substack{\text{Thermal power}\\ \text{exchange}}} \tag{6}$$

where e is the melt pool specific internal energy, measured with respect to the ambient temperature (W/kg), e_f is the specific internal energy, measured with respect to the ambient temperature, of the cold material being added to the melt pool (W/kg), e_b is the specific internal energy of the solidified bead material leaving the melt pool (W/kg), and ΣP_s is the total thermal power exchange at the melt pool boundary (W). The melt pool internal energy is

$$e(t) = c_s\left(T_m - T_\infty\right) + L + c_l\left(T(t) - T_m\right) \tag{7}$$

where c_s is the specific heat of the solid material (J/kg•K), T_m is the material melt temperature (K), T_∞ is the ambient temperature (K), c_l is the specific heat of the molten material (J/kg•K), L is the specific latent heat of fusion (solidification) (J/kg), and T is the

average melt pool temperature (K). The specific energy of the material leaving the melt pool is

$$e_b = c_s\left(T_m - T_\infty\right) \tag{8}$$

The powder added to the melt pool is assumed to not undergo significant preheating before entering the melt pool, thus, e_f = 0. With the assumed ellipsoid melt pool geometry, the substrate interface area and the free surface area from which heat convection and radiation to the ambient occurs, respectively, are

$$A_s\left(t\right) = \frac{\pi}{4} w(t) l(t) \tag{9}$$

$$A_G\left(t\right) = \frac{\pi}{\sqrt[3]{2}} \left(w(t) h(t) l(t)\right)^{2/3} \tag{10}$$

The total thermal power exchange at the melt pool boundary is

$$\begin{aligned} \sum P_s\left(t\right) = & \underbrace{\eta Q(t)}_{\substack{\text{Laser power} \\ \text{into melt pool}}} - \underbrace{A_s\left(t\right)\alpha_s\left(T\left(t\right) - T_m\right)}_{\substack{\text{Conductive heat loss to previous} \\ \text{layers}}} \\ & - \underbrace{A_G\left(t\right)\alpha_G\left(T\left(t\right) - T_\infty\right)}_{\substack{\text{Convective heat loss to} \\ \text{ambient atmosphere}}} - \underbrace{A_G\left(t\right)\varepsilon\sigma\left(T\left(t\right)^4 - T_\infty^4\right)}_{\substack{\text{Radiative heat loss to} \\ \text{ambient atmosphere}}} \end{aligned} \tag{11}$$

where η is the laser-surface coupling efficiency, Q is the laser power (W), α_s is the convection coefficient of heat transfer in the direction of the substrate (W/m^{2}K), α_G is the

convection coefficient for heat losses due to gaseous convection (W/m^2K), ε is the melt surface emissivity, and σ is the Stefan-Boltzmann constant (W/m^2K^4). Note that a term describing heat transfer effects through previous layers to the substrate in the z-direction is not included in Eq. (11). A description of those effects would be possible by incorporating a solidification rate equation in the z-direction, similar to that described in the next section. Currently, the second term in Eq. (10) only describes conductive losses to the single previous layer in the z-direction.

3. MOVING BOUNDARY MODEL

At the boundary between two phases, physical properties can suffer from discontinuities. This physical phenomenon was first described by Jožef Stefan in 1891 to explain the rate of freezing in sea ice. Here it is used to describe the rate of change of solidification of the melt pool in the deposition direction. The rate of single phase solidification in the x-direction is [15]

$$\dot{s}(t) = \frac{k_s}{\rho L}\frac{\partial T_S(x,t)}{\partial x(t)}\bigg|_{x(t)=s(t)} - \frac{k_m}{\rho L}\frac{\partial T_{MP}(x,t)}{\partial x(t)}\bigg|_{x(t)=s(t)} \tag{12}$$

where ρ is assumed to be temperature independent, k_m and k_s are the material thermal conductivity in the melt and solid regions (W/m-K), respectively, and T_S and T_{MP} are the solid region and melt pool temperatures (K), respectively. The temperature gradients are evaluated at the melt-solid boundary. Figure 2 shows a schematic of the temperature

gradients at the solidification boundary. The x-axis represents the position in the x-direction as denoted in Fig. 2.

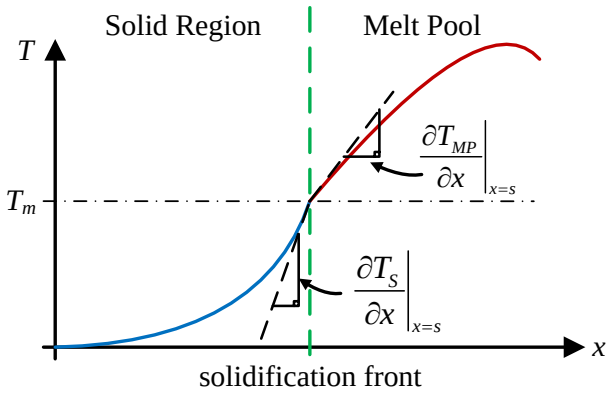

FIG. 2. SCHEMATIC SHOWING SOLID-MELT PHASE CHANGE BOUNDARY AND SOLID REGION AND MELT POOL TEMPERATURE GRADIENTS.

3.1. DETERMINATION OF TEMPERATURE GRADIENTS

To model the time-varying evolution of the melt pool solidification front using the Stefan equation (Eq. (12)), knowledge of the temperature gradients in both the solid and melt regions is needed. However, measuring both the solid and melt region temperature gradients is challenging. Some current measurement techniques of melt pool temperature include infrared temperature sensors and thermal imaging cameras [16]. While the latter could be used to measure the melt pool size and shape, thermal cameras are expensive and require substantial image processing to determine temperature gradients. Furthermore, they can only measure temperature gradient of the melt pool surface, whereas the gradient at the melt pool-solid interface is needed. Information about the solid region temperature gradient can be approximated using a finite difference analysis,

while knowledge of the melt pool gradient can be obtained from a steady state one dimensional heat equation model of the melt pool.

3.1.1. Melt Region. The melt pool gradient is approximated from the steady state analysis of one dimensional conduction in the x-direction with lumped thermal power terms. The motivation behind posing the problem as such is that it provides a relatively simple shape function for the melt pool gradient, while still permitting the dynamic melt pool model to capture the transient effects associated with the melt pool length and temperature. Figure 3 shows a schematic of the melt pool moving with scan speed v, having laser power input Q_{laser}, and lumped thermal losses, along with a schematic of the melt pool temperature profile.

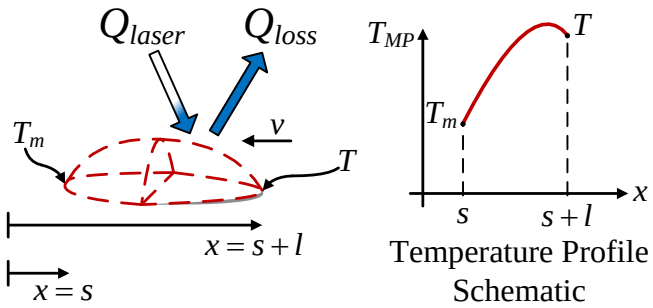

FIG. 3. SCHEMATIC OF 1D CONDUCTION IN MELT POOL WITH HEAT GENERATION FROM LASER AND MELT POOL TEMPERATURE PROFILE.

Using the average melt pool temperature as the boundary condition for the internal melt pool temperature at $x = s + l$ and the material melting temperature as a lower bound on the internal melt pool temperature, the boundary conditions are

$$\begin{aligned} T_{MP}\left(s,t\right) &= T_m \\ T_{MP}\left(s+l,t\right) &= T \end{aligned} \tag{13}$$

Note that the actual maximum internal melt pool temperature may be larger than the average melt pool temperature. The governing equation of the problem in Fig. 3 is

$$k_m \frac{\partial^2 T_{MP}\left(x,t\right)}{\partial x\left(t\right)^2} = -\frac{Q_{lumped}\left(t\right)}{V\left(t\right)} \tag{14}$$

where Q_{lumped} is

$$\begin{aligned} Q_{lumped}\left(t\right) &= Q_{input}\left(t\right) - Q_{loss}\left(t\right) \\ &= \underbrace{\eta Q\left(t\right)}_{\text{Power input from laser}} - \underbrace{A_G\left(t\right)\alpha_G\left(T\left(t\right)-T_\infty\right)}_{\text{Convective losses to the ambient}} \\ &\quad - \underbrace{A_G\left(t\right)\varepsilon\sigma\left(T\left(t\right)^4 - T_\infty^4\right)}_{\text{Radiative losses to the ambient}} - \underbrace{A_s\left(t\right)\alpha_M\left(T\left(t\right)-T_m\right)}_{\text{Conductive losses in the substrate direction}} \end{aligned} \tag{15}$$

where α_M is the solidification rate coefficient of conduction in the direction of the substrate (W/m^2K). This term differs from the one defined in Eq. (11) in that it accounts for less of the total conduction from the melt pool. The conduction coefficient in Eq. (11) accounts for conduction in both the deposition direction and in the vertical direction, as there is no term describing conduction in the deposition direction. Here, the conduction coefficient only captures conduction in the vertical direction. Integrating Eq. (14) twice

and using the boundary conditions in Eq. (13), the melt pool temperature shape function is

$$\begin{aligned} T_{MP}(x,t) = & -\frac{Q_{lumped}(t)}{2k_m V(t)} x(t)^2 \\ & + \left[\frac{T(t)-T_m}{l(t)} + \frac{Q_{lumped}(t)}{2k_m V(t)} \left(2s(t)+l(t)\right) \right] x(t) \\ & - \frac{Q_{lumped}(t)}{2k_m V(t)} s(t)\left(s(t)+l(t)\right) - \frac{T(t)-T_m}{l(t)} s(t) + T_m \end{aligned} \tag{16}$$

To determine the melt pool temperature gradient at the solidification front, Eq. (16) is differentiated with respect to x and evaluated at the solid-melt interface, $x = s$, yielding

$$\begin{aligned} \left.\frac{\partial T_{MP}(x,t)}{\partial x}\right|_{x=s} &= -\frac{Q_{lumped}(t)}{k_m V(t)} l(t) + \frac{T(t)-T_m}{l(t)} \\ &= G_{MP}\left(T(t), \dot{m}(t), Q(t), l(t), w(t), h(t)\right) \end{aligned} \tag{17}$$

3.1.2. Solid Region. Determining the temperature profile in a typical thin-walled part built using LMD can be simplified by assuming uniform temperature distribution in the y-direction (i.e., along the width). In most depositions, the length of the formed structure is much larger than the track width and, for multi-layer deposits, the track height is much larger than the track width as well. Therefore, when building parts vertically, the amount of heat flowing in the x- and z-directions is larger than the heat flowing in the y-direction. Using a finite element analysis of a semi-infinite 2D structure

moving with a velocity *v*, the solid region temperature gradient can be calculated at the solidification boundary. The finite element part setup is shown in Fig. 4, where the deposited track is the material that has been solidified during the current deposition layer and the track height, *H*, is the height of the solidified material, not including the current layer. The dashed lines represent previously built layers. The heat source is fixed at a position with its center coinciding with the center of the melt pool and the part moves in the negative x-direction with a scan speed *v*.

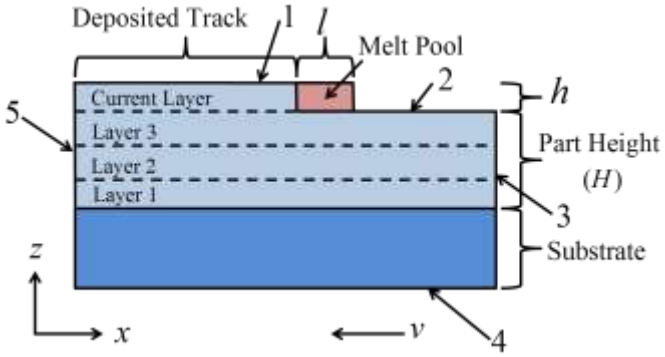

FIG. 4. SCHEMATIC SHOWING FINITE DIFFERENCE ANALYSIS SETUP FOR SOLID REGION TEMPERATURE GRADIENT DETERMINATION.

The melt pool in the finite difference analysis is defined by an area that is held at a constant temperature, $T(x,z,t) = T_m$. Free convection and radiation to the ambient is prescribed on the two top surfaces, labeled 1 and 2 in Fig. 4. For many setups, the substrate is merely clamped in place on the edges and the bottom of the substrate is exposed to ambient air. Thus, free convection and radiation to the ambient is also used on the bottom surface, labeled 4 in Fig. 4. A picture of this setup is shown in Fig. 5. It

should be noted that while there is free convection on the substrate bottom for the current experimental setup, this is not always true. If the bottom of the substrate in the fixture is mated to a large metal block, or some other setup, a free convection and radiation boundary condition on surface 4 in Fig. 4 would no longer be accurate.

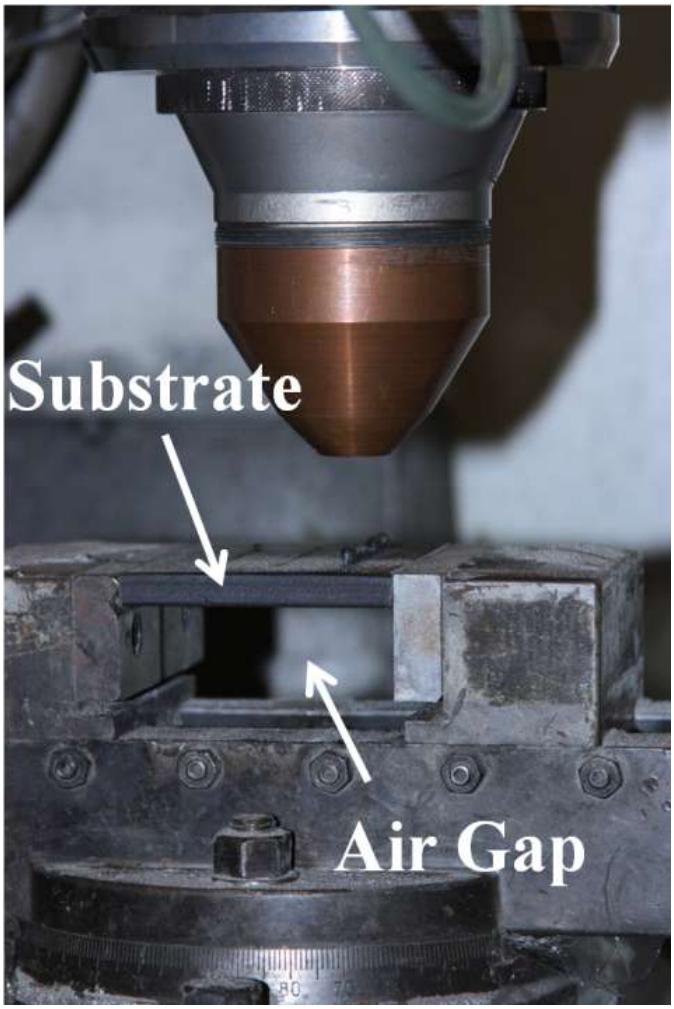

FIG. 5. PHOTOGRAPH SHOWING A SUBSTRATE CLAMPED IN A FIXTURE WITH AN AIR GAP BELOW THE SUBSTRATE ALLOWING FOR FREE CONVECTION.

Although a uniform temperature distribution in the y-direction is assumed for the part in the finite difference analysis, the substrate does not exhibit the same behavior. Conduction in the y-direction in the substrate becomes much more significant because of the dimensional difference in the y-direction between the part being built and the substrate. Modeling the entire substrate in the finite difference analysis would require a projection into three dimensions and thus the computational complexity of the finite difference analysis would substantially increase. However, keeping the finite element analysis in two dimensions and applying a scaling factor ξ_{sub} to the substrate can simulate a substrate that exhibits thermal or dimensional characteristics different than those of the part. The scaling factor ξ_{sub} is applied to the thermal conductivity of the substrate as

$$\alpha_{sub} = \frac{\xi_{sub} k_s}{\rho c_s} \tag{18}$$

The two dimensional heat equation with volumetric radiation heat losses governing the thermal profile in the substrate and the part, respectively, are

$$\left(\frac{\partial T_S(x,z,t)}{\partial t} + v \frac{\partial T_S(x,z,t)}{\partial x} \right) = \alpha_{sub} \left(\frac{\partial^2 T_S(x,z,t)}{\partial x^2} + \frac{\partial^2 T_S(x,z,t)}{\partial z^2} \right) - Q_{radiation} \tag{19}$$

$$\left(\frac{\partial T_S(x,z,t)}{\partial t} + v \frac{\partial T_S(x,z,t)}{\partial x} \right) = \alpha_{part} \left(\frac{\partial^2 T_S(x,z,t)}{\partial x^2} + \frac{\partial^2 T_S(x,z,t)}{\partial z^2} \right) - Q_{radiation} \tag{20}$$

where $\alpha_{part} = k/\rho c_s$ is the part thermal diffusivity (m^2/s) and

$$Q_{radiation} = \frac{2\sigma\varepsilon}{\rho c_p w}\left(T_S^4\left(x,z,t\right) - T_\infty^4\right) \tag{21}$$

In addition to the governing equation for the substrate, ξ_{sub} is also applied to the substrate boundary conditions where applicable. Table 1 gives a summary of the equations used for the finite difference analysis and the associated areas to which the equations are applied.

TABLE 1. FINITE ELEMENT ANALYSIS EQUATIONS.

Boundary/ Area	Equation
Boundaries 1 & 2	$\alpha_{part}\frac{\partial T_S\left(x,z,t\right)}{\partial z} + q_{conv} + q_{rad} = \frac{\Delta z}{2}\left(\frac{\partial T_S\left(x,z,t\right)}{\partial t} + v\frac{\partial T_S\left(x,z,t\right)}{\partial x}\right)$ where $q_{conv} = \frac{h}{\rho c_p}\left(T_S\left(x,z,t\right) - T_\infty\right),\ q_{rad} = \frac{\varepsilon\sigma}{\rho c_p}\left(T_S^4\left(x,z,t\right) - T_\infty^4\right)$
Boundaries 3 & 5	$T_S\left(x,z,t\right) = T_\infty$
Boundary 4	$\alpha_{sub}\frac{\partial T_S\left(x,z,t\right)}{\partial z} + q_{conv} + q_{rad} = \frac{\Delta z}{2}\left(\frac{\partial T_S\left(x,z,t\right)}{\partial t} + v\frac{\partial T_S\left(x,z,t\right)}{\partial x}\right)$
Part	$\left(\frac{\partial T_S\left(x,z,t\right)}{\partial t} + v\frac{\partial T_S\left(x,z,t\right)}{\partial x}\right) = \alpha_{part}\left(\frac{\partial^2 T_S\left(x,z,t\right)}{\partial x^2} + \frac{\partial^2 T_S\left(x,z,t\right)}{\partial z^2}\right) - Q_{radiation}$
Substrate	$\left(\frac{\partial T_S\left(x,z,t\right)}{\partial t} + v\frac{\partial T_S\left(x,z,t\right)}{\partial x}\right) = \alpha_{sub}\left(\frac{\partial^2 T_S\left(x,z,t\right)}{\partial x^2} + \frac{\partial^2 T_S\left(x,z,t\right)}{\partial z^2}\right) - Q_{radiation}$
Melt Pool	$T_S\left(x,z,t\right) = T_m$

As track height increases, the role the substrate plays in absorbing thermal power from the melt pool diminishes. The temperature profiles in Fig. 6 demonstrate this effect. Each plot represents the temperature profile in a part built using H13 tool steel with v = 7 mm/s and t = 1 s where the white line denotes the top of a 10 mm thick substrate with ξ_{sub} = 50. The isotherms are in Kelvin. Notice that when H = 0.5 mm, the substrate experiences substantially more heating, as compared to when H = 10 mm. When the track height reaches some critical value, the substrate no longer has an effect on the x-direction temperature gradient.

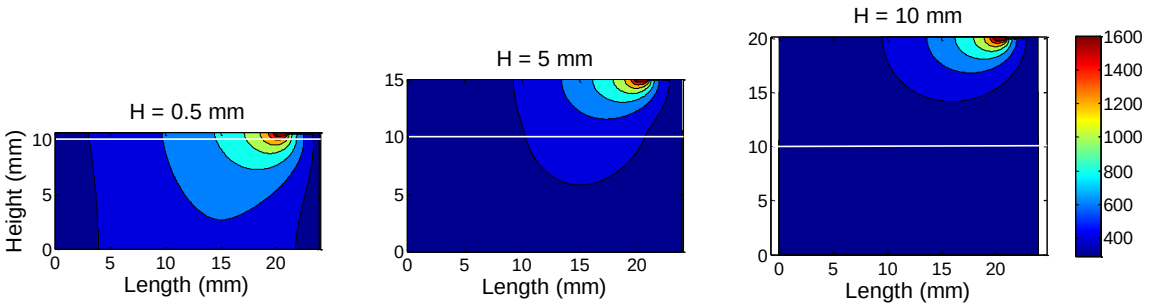

FIG. 6. TEMPERATURE CONTOUR PLOTS FOR v = 7 mm/s, ξ_{sub} = 50, AND H = 0.5, 5, AND 10 mm WHEN t = 1 s.

Additionally, as scan speed increases, there is less time for the melt pool thermal power output to heat the area immediately adjacent to the melt pool, before the heat source leaves. This allows more thermal power to be conducted in the direction of deposition, causing the spatial rate of cooling in the x-direction to be less. At lower speeds, a majority of the heat is conducted in the z-direction, causing the spatial rate of cooling in the x-direction to be larger. This effect can be seen in Fig. 7, where the scan speed ranges from v = 0.5 to 14 mm/s at a track height of H = 5 mm and t = 1 s where ξ_{sub}

= 50. At v = 0.5 mm/s, the heat from the melt pool conducts more directly into the substrate, again denoted by the white line, and less is conducted in the x-direction, as compared to when v = 14 mm/s. As with increasing height, beyond a critical value, scan speed no longer has an effect on the x-direction temperature gradient.

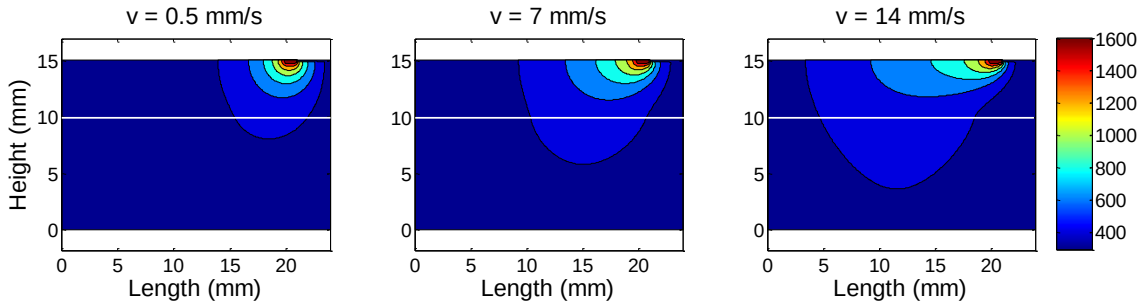

FIG. 7. TEMPERATURE CONTOUR PLOTS FOR H = 5 mm, ξ_{sub} = 50, AND v = 0.5, 7, AND 14 mm/s WHEN t = 1 s.

The trends in scan speed and track height described above are summarized in Figures 8 and 9, where the temperature gradient is plotted as a function of track height and scan speed, respectively when ξ_{sub} = 50. Although these trends hold true in general, the dynamics of the temperature gradient with respect to track height and scan speed are highly nonlinear.

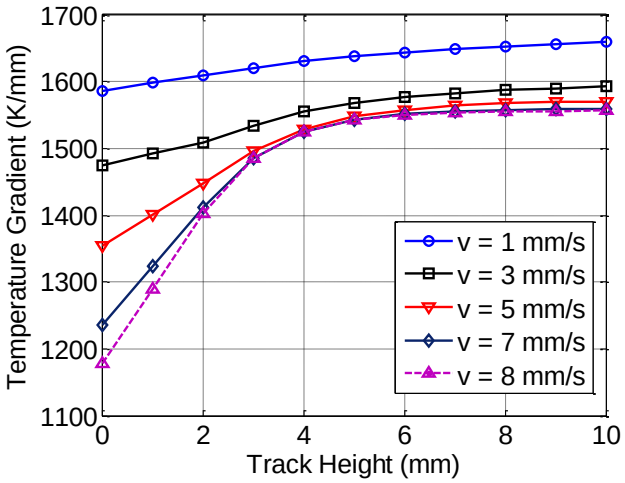

FIG. 8. X-DIRECTION STEADY STATE TEMPERATURE GRADIENT AS A FUNCTION OF TRACK HEIGHT AT VARIOUS SCAN SPEEDS.

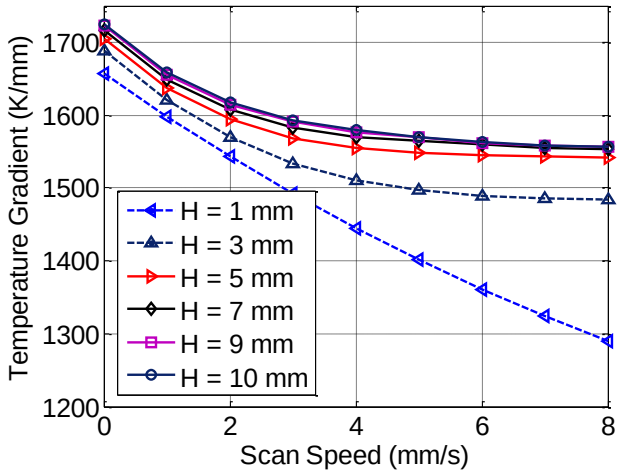

FIG. 9. X-DIRECTION STEADY STATE TEMPERATURE GRADIENT AS A FUNCTION OF SCAN SPEED AT VARIOUS TRACK HEIGHTS.

The temperature gradient formulations as described above form functions that relate the process inputs laser power, scan speed, and powder flow rate, as well as the melt pool temperature, to the quantity of interest, namely, melt pool length. The Stefan equation can now be modeled as

$$\dot{s}(t) = G_{SR}\left(v(t), H\right) - G_{MP}\left(Q(t), \dot{m}(t), T(t), l(t), w(t), h(t)\right) \qquad (22)$$

where G_{MP} is the function described by Eq. (17) and G_{SR} is the value calculated from the solution of the finite element analysis for a given scan speed and track height, as shown in Figs. 6 and 7. The function G_{SR} is implemented with a look-up table with linear interpolation between data points for a given scan speed.

4. MODEL VALIDATION

4.1. EXPERIMENTAL SYSTEM SETUP

The LMD setup utilized for the experimental work conducted in this paper consists of a 5-axis FADAL CNC machine, a blown-powder delivery system, a 1kW diode laser and a National Instruments (NI) real-time control system. The NI system is used to input signals to the powder feeder and laser. A tool path programmed in the CNC G-code is used to move the CNC machine x-y table while an interface in LabView is used to synchronize the motion with the powder feeder and laser.

4.2. WIDTH VALIDATION

As seen in [12], when depositing using H13 tool steel, the melt pool dimensions are influenced by track height. Additionally, in the previous section, it is seen that the substrate affects the deposition dimensions through the value of ξ_{sub}. Using the process parameters used in Table 2, two 60 mm long thin-walled tracks are deposited, one on a substrate with a larger ξ_{sub} value, deposit 1 in Fig. 10, and than the other, deposit 2 in Fig.

10. The difference in ξ_{sub} values is a consequence of their size differences. Deposit 1 was built in 15 layers while deposit 2 was built in 40 layers.

TABLE 2. EXPERIMENTAL PROCESS PARAMETERS.

Process Parameter	**Value**
Laser Power, Q (W)	600
Scan Speed, v (mm/s)	2.54
Powder Flow Rate, $\dot{m}$ (g/min)	3.73
Track Length, L_t (mm)	60

FIG. 10. DEPOSITS ON SUBSTRATES WITH A LARGE ξ_{sub} VALUE (1) AND A SMALL ξ_{sub} VALUE (2).

After deposition, each structure is scanned and digitized using a NEXTENGINE 3D scanner. The scanner maps the surface features of the deposition to a point cloud consisting of (x,y,z)-tuples. At six locations along each track, a cross-sectional slice is

taken so that the width variation can be examined. These slices are shown in Figs. 11 and 12 for deposits 1and 2, respectively.

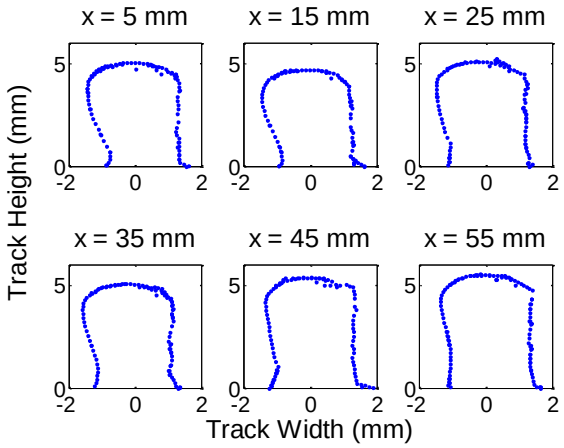

FIG. 11. CROSS-SECTIONS OF DIGITZED THIN-WALLED DEPOSIT 1 USING PROCESS PARAMETERS IN TABLE 2.

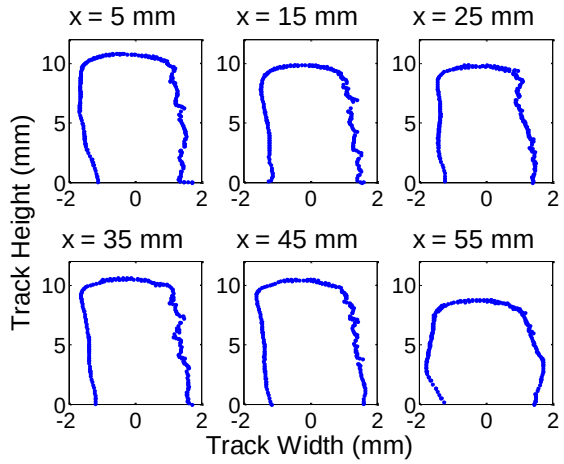

FIG. 12. CROSS-SECTIONS OF DIGITZED THIN-WALLED DEPOSIT 2 USING PROCESS PARAMETERS IN TABLE 2.

The sixth slice for deposit 2 experiences a large bulging effect not seen in the other slices for that deposit. This is most probably an artifact of the process. At the end of the tool path, the CNC machine decelerates while the powder flow rate and laser

power are still at their commanded levels. This causes a decrease in scan speed and thus a higher spatial density of powder being deposited. As layers are added, this effect is amplified, producing the large bulge in slice six of deposit 2. It should be noted, however, this does not affect the overall trend of the width change for either deposit. For deposit 1, this width change is seen in slices from the middle of the track as well as at the ends. Additionally, the smaller width change for deposit 2 is seen in all of the slices except slice six.

The finite element analysis is implemented using a fully implicit scheme. The inclusion of radiation terms causes the discretization to become nonlinear in the nodal temperatures. This is taken into account by of using the direct iteration procedure at each time step. The temperature profile in the part is calculated at each time step until the temperature gradient reaches steady state. The temperature gradient is calculated by a first order backwards difference at the boundary between the melt pool and the deposited track and averaged over the height of the melt pool. The length of the melt pool in the finite element analysis is scaled such that the thermal output in the z-direction matches what the energy balance predicts. The mesh size used for the finite element analysis is $\Delta x = \Delta z = 10$ μm and the time step for the simulation is $\Delta t = 10$ ms. The finite element analysis is conducted for a substrate thickness of 10 mm and at increasing track heights in increments of 0.5 mm with a build material of H13 tool steel. At each track height, the temperature gradient in the solid region is calculated as described in the previous section.

The process model presented above is integrated in time using a Runge-Kutta 4^{th} order scheme with a given set of initial conditions and time step $\Delta t = 10$ ms. Using a set of process parameters, material properties, model parameters, and a given temperature

gradient calculated using the FEA, the process is simulated. At the end of each simulated layer, the average track width is determined.

Using the material properties and model parameters in Table 3, the temperature gradients as a function of track height for H13 tool steel when v = 2.54 mm/s and with ξ_{sub} = 50 and ξ_{sub} = 1 are shown in Figure 13.

TABLE 3. H13 TOOL STEEL MATERIAL PARAMETERSUSED IN SIMULATION STUDIES.

Parameter	**Value**
Density, ρ (kg/m^3)	7760
Melt Temperature, T_m (K)	1730
Wetting Angle, θ (deg)	90
Specific Heat of Molten Material, c_l (J/kg-K)	480
Specific Heat of Solid Material, c_s (J/kg-K)	460
Specific Latent Heat of Fusion, L (J/kg)	2.72×10^5
Molten Material Thermal Conductivity, k_m (W/m^2-K)	43.6
Solid Material Thermal Conductivity, k_s (W/m^2-K)	40.96
Material Catchment Efficiency, μ	0.37
Ambient Temperature, T_∞ (K)	292
Energy Balance Conduction Coefficient, α_s (W/m^2-K)	1.17×10^3
Solidification Rate Conduction Coefficient, α_M (W/m^2-K)	100
Heat Transfer Coefficient, α_G (W/m^2-K)	24
Stefan-Boltzmann Constant, σ (W/m^2-K^4)	5.67×10^{-8}
Surface Emissivity, ε	0.53

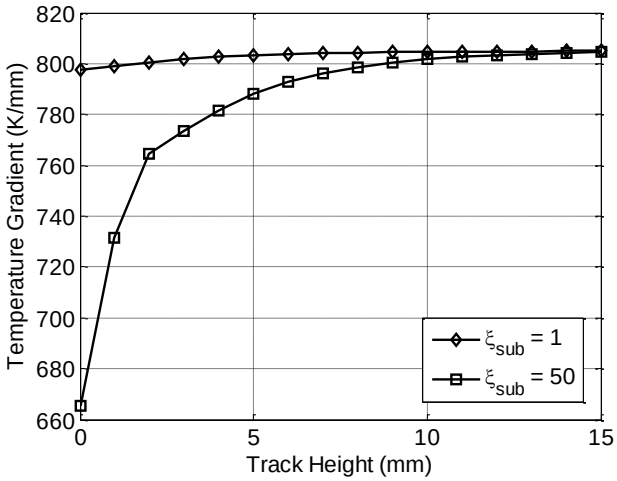

FIG. 13. SOLID REGION TEMPERATURE GRADIENTS AS A FUCNTION OF TRACK HEIGHT FOR v = 2.54 MM/S WHEN ξ_{sub} = 50 AND ξ_{sub} = 1.

The simulated width using the temperature gradients in Fig. 13 and the average width over the whole deposit are plotted as functions of track height for deposits 1 and 2 in Figs. 14 and 15, respectively.

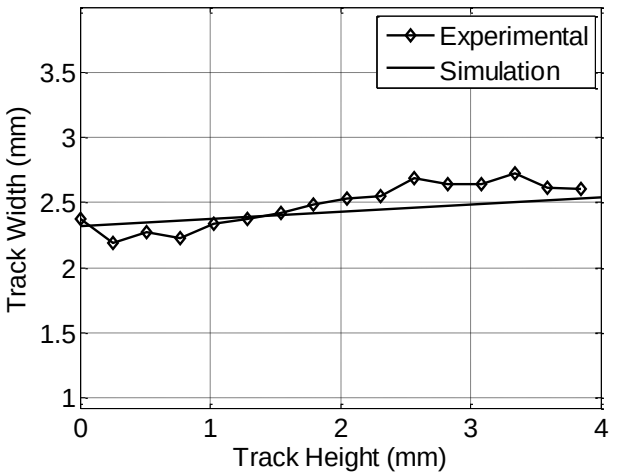

FIG. 14. WIDTH VERSUS HEIGHT AVERAGED OVER EACH DIGITIZED TRACK SLICE FOR DEPOSITION 1 AND SIMULATION DATA.

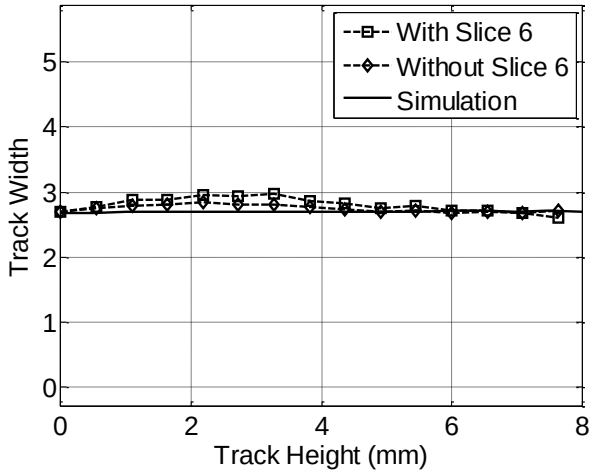

FIG. 15. WIDTH VERSUS HEIGHT AVERAGED OVER EACH DIGITIZED TRACK SLICE FOR DEPOSITION 2 AND SIMULATION DATA.

As seen in Figs. 14 and 15, the simulated track width versus track height matches very well with the experimental results. Examining deposit 1, the change in width over the height of the deposit is 0.232 mm and the change in simulated width is 0.212 mm. The root of the mean square error for the two data sets in Fig. 14 is 0.122. For deposit 2, the width change over the height of the actual deposit is 0.026 mm when excluding slice 6 and -0.104 mm when including slice 6. The simulated change in width over 8 mm is 0.042 mm. The RMSE value for the simulation data and the experimental data without slice 6 is 0.088. The RMSE values for both deposits are very close to the 0.005 inch accuracy of the NEXTENGINE 3D scanner. These results are summarized in Table 4 and show how the choice of substrate can affect melt pool morphology and that the presented model can accurately predict this effect.

TABLE 4. ACTUAL AND SIMULATED CHANGE IN WIDTH OVER HEIGHT OF DEPOSIT.

Deposit Number	Actual Change (mm)	Simulated Change (mm)	RMSE
1	0.232	0.212	0.122
2	0.026 (-0.104)	0.042	0.088

4.3. WIDTH-PROCESS PARAMETER SENSITIVITY ANALYSIS

The introduction of the solidification rate term is able to describe the change in track width as track height increases, as seen in the experimental depositions. Additionally, as formulated, the solidification rate equation incorporates all three process inputs. In order to analyze the sensitivity of the width change to process parameters, combinations of scan speed, laser power and powder flow rate were chosen over an operating range and their effects on the change in melt pool width are observed. This operating range is given in Table 5.

TABLE 5. PROCESS PARAMETER OPERATING RANGES FOR WIDTH SENSITIVITY ANALYSIS.

Process Parameter	Range
Laser Power, Q (W)	600-1000
Powder Flow Rate, $\dot{m}$ (g/min)	1-14
Scan Speed, v (mm/s)	1-8

As the process parameters are varied across their operating ranges, the percent change in track width over 10 mm of track height is recorded. After 10 mm, the change in melt pool dimensions becomes negligible because the previously built layers dictate the heat transfer from the melt pool and the substrate no longer has an effect on the temperature gradient, and thus, no effect on the melt pool dimensions. The trends for Q =

600, 800, and 1000 W over the range of scan speeds and powder flow rates given in Table 4 are shown in Figs. 16, 17, and 18, respectively.

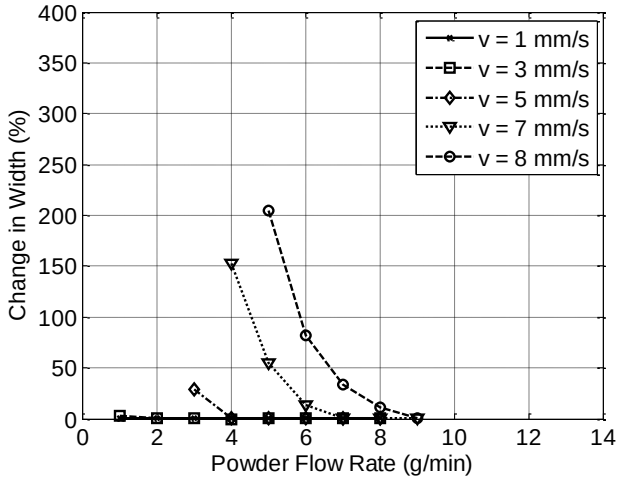

FIG. 16. PERCENT CHANGE IN TRACK WIDTH AS POWDER FLOW RATE AND SCAN SPEED VARY FOR *Q* = 600 W.

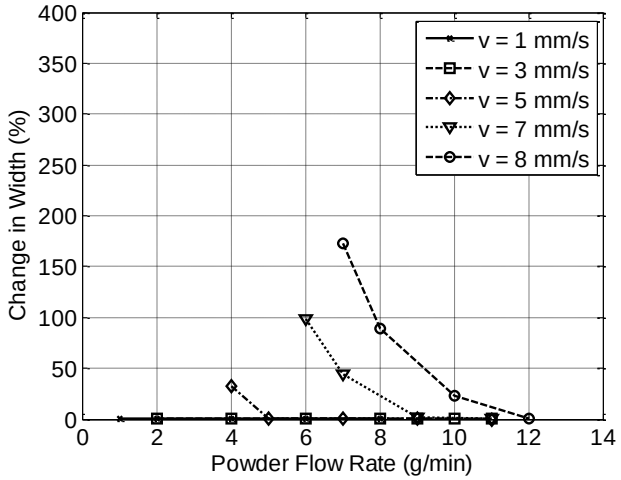

FIG. 17. PERCENT CHANGE IN TRACK WIDTH AS POWDER FLOW RATE AND SCAN SPEED VARY FOR *Q* = 800 W.

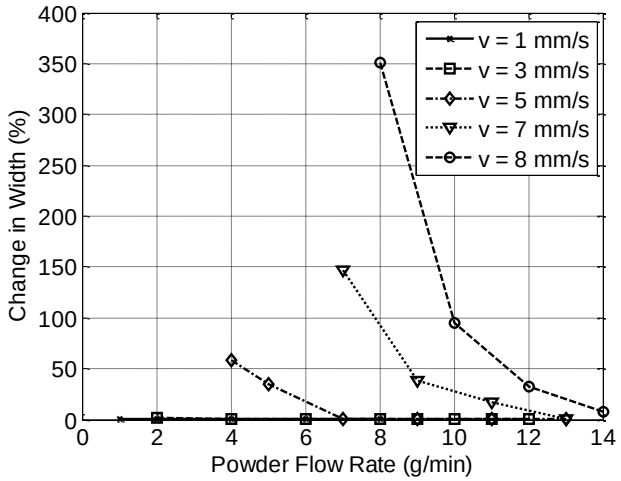

FIG. 18. PERCENT CHANGE IN TRACK WIDTH AS POWDER FLOW RATE AND SCAN SPEED VARY FOR *Q* = 1000 W.

Figures 16-17 indicate that the change in width becomes more sensitive as scan speed increases for a given powder flow rate and laser power. This is also true as laser power increases, holding scan speed and powder flow rate constant. Additionally, at a given constant scan speed and laser power, the track width change becomes less sensitive as powder flow rate increases.

As scan speed increases, when depositing a bead directly onto the substrate, the melt pool has increasingly less time to expand in the width direction before solidifying. However, as layer number increases, the bead is able to stay molten for a longer period of time, thus allowing the melt pool to expand in the width direction more before solidifying. This leads to a larger change in width over the height of a deposit.

A similar phenomenon happens when laser power increases. For lower laser powers, the amount of heat transfer from the melt pool into the substrate and then, as layers are built, the previous layers, are closer in value than for higher laser powers. Therefore, for lower laser powers, the rate of solidification in the width direction for the

first layer (depositing directly on the substrate) and for the subsequent layers is relatively close and the width does not vary as much as track height increases. For higher laser powers, a heavier thermal load is placed on conduction through the previous layers and thus the melt pool stays molten longer, before solidification, than on the first layer, allowing for flow in the width direction, and thus an increase in track width.

When powder flow rates are smaller, the amount of thermal power of the melt pool absorbed by the incoming powder is less than when powder flow rates are high. Thus, as with higher laser powers, the conduction from the melt pool through previous layers limits the amount of heat being drawn from the melt pool and allows for the melt pool to stay molten longer before solidification, again causing an increase in track width. With higher powder flow rates, the amount of heat absorbed by the incoming powder is larger and less heat is conducted from the melt pool than with lower powder flow rates. This effect causes the process dynamic across layer number to be less dramatic and in turn, a less dramatic change in melt pool width.

In practice, the melt pool size and thus track width is heavily influenced by the laser beam diameter and powder flow focus area. If the initial melt pool formed on the substrate is smaller than the powder flow focus area, a large amount of powder will fall outside of the melt pool, the catchment efficiency of the melt pool will drop significantly, and the formed bead will not grow as predicted. However, when the powder flow focus area is smaller or equal to the size of the initial melt pool, the formed bead will grow similarly to the predicted results. When scan speeds are large, the initial melt pool tends to elongate in the deposition direction and thus shrink in the width direction narrowing

the melt pool towards the dimensions of the powder flow focus area. The opposite is true as lower scan speeds.

At some combinations of laser power, powder flow rate, and scan speed, the process model breaks down and the simulation becomes unstable. These breakdowns may represent the physical limits of the process. In general, the area left of the curves in each plot represents a region of infeasibility, as this is where the simulation becomes unstable. As scan speeds increase, a higher powder flow rate is needed to add enough powder to the melt pool to form a bead. Additionally, as laser power increases, more powder is needed to absorb the power incident on the substrate to prevent ablation and allow for the formation of a molten bead. However, the model is sensitive to changes in parameter values and care should be taken to use appropriate values for the energy balance conduction coefficient, solid-liquid and liquid-gas surface tension coefficients and reasonable values for the powder catchment efficiency and laser efficiency. These parameters, while modeled as constants, are most likely in reality temperature, time and layer height dependent and the model seems most sensitive to changes in the values for these parameters.

After a uncertainty to model parameter values study is conducted, and the process and model parameters are known to some degree of accuracy, this sensitivity analysis can aid in process planning. Having knowledge of what combinations of process parameters induces the largest melt pool dimensional change can help operators avoid those areas of the operating space, account for these effects by changing process parameters from layer to layer, or utilize these effects to build complex shapes during deposition.

5. CONCLUSIONS

A height dependent LMD process model was developed in this paper. The model dynamically relates process inputs (e.g., laser power, material mass flow rate, and scan speed) to the melt pool dimensions and temperature. The model extends previous work by incorporating an equation that describes the solidification rate of the melt pool in the direction of deposition, which is comprised of the scaled difference between the solid and melt region temperature gradients. A finite element analysis was then conducted to determine the effect of scan speed and track height on the solid region temperature gradient at the melt pool solidification boundary. Simulation results were compared to experimental data and illustrate that the model is able to successfully predict changes in melt pool width as track height increases, which single layer models cannot. The results also show that the model is able to predict the effect of substrate size on the melt pool dimensions. An analysis of the sensitivity of melt pool width change to process parameters was carried out. Melt pool width is most sensitive to high laser powers, high scan speeds and lower powder flow rates.

The model developed in this paper is versatile. Since little is assumed about the process or material being deposited, the model can be utilized for various LMD setups and materials. Additionally, it has the advantage of being able to capture height dependent effects while maintaining the simplicity of the model from which it was extended. This bodes well for use in closed-loop process controller design. Additionally, the bead morphology predicted by the model allows for more dimensionally accurate structures to be fabricated using LMD.

However, further work is needed to develop a method to determine the value of ξ_{sub} for a given substrate. It has been shown that it is an important parameter in determining melt pool dimensions when the distance between the melt pool and the substrate is small.

6. REFERENCES

[1] Choi, J., 2002, "Process and Properties Control in Laser Aided Direct Metal/Materials Deposition Process," *Proceedings of IMECE*, New Orleans, LA, November 17-22, pp. 1-9.

[2] Doumanidis, C. and Kwak, Y-M., 2001, "Geometry Modeling and Control by Infrared and Laser Sensing in Thermal Manufacturing with Material Deposition," *ASME Journal of Manufacturing Science and Engineering*, Vol. 123, pp. 45–52.

[3] Kaplan, A.F.H. and Groboth, G., 2001, "Process Analysis of Laser Beam Cladding," *ASME Journal of Manufacturing Science and Engineering*, Vol. 123, pp. 609-613.

[4] Han, L., Liou, F.W., and Musti, S., 2005, "Thermal Behavior and Geometry Model of Melt Pool in Laser Material Process," *ASME Journal of Heat Transfer*, Vol. 127, pp. 1005-1014.

[5] Pinkerton, A. and Li, L., 2004, "Modelling the Geometry of a Moving Laser Melt Pool and Deposition Track vie Energy and Mass Balances," *Journal of Physics D: Applied Physics*, Vol. 37, pp. 1885-1895.

[6] Bennon, W. and Incropera, F., 1987, "A Continuum Model for Momentum, Heat, and Species Transport in Binary Solid-Liquid Phase Change Systems I," *International Journal of Heat Mass Transfer*, Vol. 30, pp. 2171-2187.

[7] Bennon, W. and Incropera, F., 1987, "A Continuum Model for Momentum, Heat, and Species Transport in Binary Solid-Liquid Phase Change Systems II," *International Journal of Heat Mass Transfer*, Vol. 30, pp. 2161-2170.

[8] Hua, Y. and Choi, J., 2005, "Adaptive Direct Metal/Material Deposition Process Using a Fuzzy Logic-based Controller," *Journal of Laser Applications*, Vol. 17, pp. 200-210.

[9] Choi, J. and Chang, Y., 2006, "Analysis of Laser Control Effects for Direct Metal Deposition Process," *Journal of Mechanical Science and Technology*, Vol. 20, pp. 1680-1690.

[10] Fathi, A., Khajepour, A., Toyserkani, E., and Durali, M., 2007, "Clad Height Control in Laser Solid Freeform Fabrication Using a Feedforward PID Controller," *International Journal of Advanced Manufacturing Technology*, Vol. 35, pp. 280-292.

[11] Fathi, A., Khajepour, A., Durali, M., and Toyserkani, E., 2008, "Geometry Control of the Deposited Layer in a Nonplanar Laser Cladding Process Using a Variable Structure Controller," *ASME Journal of Manufacturing Science and Engineering*, Vol. 130, pp. 031003:1-11.

[12] Tang, L. and Landers, R.G., 2011, "Layer-to-Layer Height Control for Laser Metal Deposition Process," *ASME Journal of Manufacturing Science and Engineering*, Vol. 133, pp. 021009:1-9.

[13] Esser, W.G. and Walter, R., 1981, "Heat Transfer and Penetration Mechanisms with GMA and Plasma GMA Welding," *Welding Journal*, Vol. 60, pp. 37s-42s.

[14] Thorn, K., Feenstra, M., Young, J.C., Lawson, W.H.S., and Kerr, H.W., 1982, "The Interaction of Process Variables-Their Influence on Weld Dimensions in GMA Welds on Steel Plates," *Metal Construction*, Vol. 14, pp. 128-133.

[15] Crank, J., 1984, *Free and Moving Boundary Problems*, Clarendon Press, London, UK.

[16] Meriaudeau, F. and Truchetet, F., 1996, "Control and Optimization of the Laser Cladding Process using Matrix Cameras and Image Processing," *Journal of Laser Applications*, Vol. 8, pp. 317-324.

VITA

Patrick M. Sammons was born in Bridgeton, Missouri, USA on August 6, 1986. In December 2009, he received his B.S. in Mechanical Engineering from the University of Missouri, Columbia, Missouri, USA. In August 2012, he received his Master of Science degree in Mechanical Engineering from the Missouri University of Science and Technology, Rolla, Missouri, USA.

He has published and presented a conference paper at the ASME International Symposium on Flexible Automation. Patrick M. Sammons is also a member of both the Institute of Electrical and Electronics Engineers (IEEE) and the American Society of Mechanical Engineers (ASME).